973
国家重点基础研究发展计划

Theory and Application for Retrieval and Fusion of Quantitative Spatial and Temporal Information from Complex Natural Environment

复杂自然环境时空定量信息的获取与融合处理的理论和应用

金亚秋 主编

上海科学技术出版社

Theory and Application for

Retrieval and Fusion of

Quantitative Spatial and

Temporal Information from

Complex Natural Environment

金亚秋 主编

复杂自然环境时空定量信息的获取与融合处理的理论和应用

上海科学技术出版社

内容提要

自然环境正由于复杂，所以才丰富多彩。而要解读自然界这本“天书”，需借助于来自环境的“真实”信息。复旦大学金亚秋教授和他的研究团队，长期致力于从海量的遥感数据中寻求定量科学信息，探求人类自身生存环境的变化规律的研究工作，在遥感信息机理，特别是电磁波谱在复杂自然环境条件下的动力学规律的探索方面，进行了系统而有效的工作，获得了骄人的成绩，提出了许多新理论、新方法。将他们近年来发表于国内外各著名相关杂志的科研成果结集出版，有助于读者了解他们的研究过程和该领域研究的新进展。本书可供信息科学、地球科学等领域的科研人员参考，也可供大专院校相关专业的师生阅读。

图书在版编目(CIP)数据

复杂自然环境时空定量信息的获取与融合处理的理论和应用/金亚秋主编. —上海：上海科学技术出版社，2005.12
ISBN 7-5323-8175-7

Ⅰ.复... Ⅱ.金... Ⅲ.遥感技术—应用—大地测量—信息处理 Ⅳ.P237

中国版本图书馆 CIP 数据核字(2005)第 090773 号

审图号：CS(2005)796 号

责任编辑 戚越然
装帧设计 陈 蕾

上海世纪出版股份有限公司
上 海 科 学 技 术 出 版 社 出版、发行
(上海市钦州南路 71 号 邮编 200235)
新华书店上海发行所经销
苏州望电印刷有限公司印刷
开本 889×1194 1/16 印张 34.5 字数 1200 千字
2005 年 12 月第 1 版 2005 年 12 月第 1 次印刷
印数：1—1 100
ISBN 7-5323-8175-7/N·230
定价：120.00 元

序

复旦大学金亚秋教授率领他的研究团队，对遥感信息机理，特别是电磁波谱在复杂自然环境条件下的动力学规律，进行了长期的、系统的实证与验证研究，出版了一系列专著。在这部论文集中，他们又承前启后，汇集了有关遥感信息流程中分析处理阶段的重要理论和方法，涉及大气验证、水文过程、地—海目标特性，以及多源信息融合、人工智能技术等复杂的技术关键科学问题，提出了许多遥感信息的新理念、新方法。引人入胜，读来令人耳目一新。

自然环境正由于它如此复杂，所以丰富多彩，引无数科技精英竞折腰！在苍茫宇宙中，我们所能看到的明物质只占其中4%，而暗物质和暗能量各占23%和73%。我们人类只对明物质的一部分运动规律有了一定的认识，又仅占其中的4%！对于复杂的自然界这部“天书”，人类还只能说知之甚少，还不敢说知之甚多。牛顿定律实现了人类认知自然的第一次大飞跃；200年之后，爱因斯坦的相对论问世，又一次突破了宏观、低速运动的局限，实现了再一次飞跃。科学发展是一个接力跑的过程，科学技术问题不断通过实践与验证，才会更加逼近真理；复杂性问题的理论诠释和技术解决方案正是科技工作中的难点和亮点，但并不是不可看的盲区。科学认知永远不会停顿，而是螺旋式前进着。即由低级的简单到复杂，再由低级的复杂上升到高级的简单。

自然环境是一个开放的、复杂的巨系统，成千上万的复杂性问题纵横交织在一起，构成许多子系统。牵一发而动千钧，要想解决其中的任何一个复杂问题，首先需要逐个理顺它在整个系统中的内在与外在的联系和运动规律。遥感信息来自自然环境，经过时空定量分析，从而模拟自然环境现状，反馈过去，预测未来。我们也必须遵循系统集成的科学方法，首先针对其中一些基础性的复杂问题，逐一掌握它的动力学特征；摸清它与环境之间存在的物质、能量、信息交换的过程，以及人类的参与和影响。然后把它作为复杂系统中的一个“组件”，嵌入到复杂系统中去。再由若干复杂系统综合集成为开放的巨系统，借助于网络与数据库，通过人机互动、合作，建立可操作的智能化平台，是有可能得到解决的（参见戴汝为2005年的文章）。例如复杂的天气系统、复杂的数字城市系统、灾害评估预警系统等诸多领域，都已经取得了突破性的进展。

在天、空、地一体化的正确方针指引下，在资源环境系列卫星逐步业务化的基础上，加强统筹规划，系统集成，组建公用信息平台，拓展接收台站网络。我们相信，遥感信息复杂流程的现代化是指日可待的。当前最迫切企盼的，就是像金亚秋教授和他的研究团队所从事的深入的、系统的应用基础研究工作。有了来自多学科、不同视角的应用基础研究成果；集中智慧，依托新一代网络系统和高性能节点的支持，遥感信息所面对的自然环境复杂性问题，必然是会逐步迎刃而解的。从这部论文集的出版，我们看到了曙光，谨此表示热烈的祝贺。

中国科学院资深院士 陈述彭

二〇〇五年“五一”节日

前言

国家重点基础研究计划项目2001CB309400“复杂自然环境时空定量信息的获取与融合处理的理论和应用”包括六个课题：2001CB309401 空间遥感散射辐射传输机理与信息获取（课题负责人：金亚秋，复旦大学）；（2）2001CB309402 空间微波遥感地（海）表和大气数据验证（课题负责人：陈洪滨，中科院大气物理所；张文建，国家卫星气象中心）；（3）2001CB309403 多源数据融合的理论、算法与应用（课题负责人：韩崇昭，西安交通大学）；（4）2001CB309404 中国水圈环境关键与典型事件时空尺度定量遥感信息系统与应用示范（课题负责人：李新，中科院兰州寒区旱区工程研究所；张万昌，南京大学）；（5）2001CB309405 目标与环境共存时的信息获取（课题负责人：金亚秋，复旦大学；韩崇昭，赵广社，西安交通大学）；（6）2001CB309406 SAR 和 InSAR 的信息应用（课题负责人：王超，中科院遥感所）。

该项目提出：面对空间遥感高科技的发展与信息时代的到来，面对国家对自然环境信息的各种重大需求，从海量遥感数据寻求定量的科学的信息，探求人类自身生存环境的变化规律，占据国际信息科技与地球系统科学交叉发展前沿一席之地，为中国的发展服务。

我们从电磁波与复杂自然环境相互作用的遥感信息机理研究出发，以复杂环境散射辐射信息建模与数值模拟作为科学理论支撑，以求对当今与未来空间遥感信息研究的发展有显著的贡献。

利用遥感数据图像资源，提出空间遥感数据标定验证与多源信息融合的有效新手段与新方法，实现大气、陆地、海洋、目标与环境遥感科学信息的获取与处理，满足国家持续发展的需求。

建立富有中国科学家创新特点的复杂自然环境时空定量信息的前沿基础理论与数值模拟；形成空间遥感数据验证、信息获取与融合处理的有效方法。

解决我国国民经济持续发展对于水圈环境（大气、陆地、海洋）估算、监测、保护与开发所提出的若干重大环境信息问题，满足应用部门对这类问题的需求；解决环境与目标共存信息获取与处理的若干重要问题。

发展信息科技与地球科学的交叉，建立高水平的中国中青年科学家队伍。

经过三年的努力，在以上预定目标上已取得了不少重要的成果，通过了项目的中期评估。我们在空间遥感若干前沿问题上取得了十分有意义的成果，与国内其他重要的国家科研与应用项目有了进一步的衔接与扩展，主编了《电波科学学报》的“空间电磁波遥感信息获取与处理”专刊（2004 年第 19 卷第 4 期），《加拿大遥感杂志》（Canadian Journal of Remote Sensing）的“水资源遥感研究”专刊（2004 年第 30 卷第 5 期），主编了由国内外专家撰写的专著《Wave Propagation, Scattering and Emission in Complex Media》（新加坡世界科技出版社和北京科学出版社共同出版，2004），集中地反映了我们项目的一部分研究成果。我们申报了中国与美国的发明专利。此外我们举办了多次国内与国际学术研讨会，进一步充实了我们的研究内容，也扩大了中国科学工作者在这一领域的国内外影响。

由于相当一部分论文散见在国内外各种学术刊物上，特别是本项目覆盖的学科领域相当广泛，各课题研究的方式与对象都有不同，平时也几乎没有人能翻阅所有这些刊物。为总结本项目的研究成果，能在空间遥感大科学的角度上看待多学科的交叉融合，使得本项目后两年的研究更上一层楼；同时让国内科学研究者，特别是青年学者与研究生们，了解整个项目的研究进展，共同发展中国的遥感科学事业，我们选择了一批已发表的学术刊物论文汇编成本书。希望这是“抛砖引玉”，能引来中国空间遥感信息科学技术的更大更兴旺的发展。

本书的第一章“遥感机理与遥感信息理论”论述空间遥感信息机理，地球环境极化电磁散射与辐射传输的理论建模、数值模拟，以及遥感信息获取的新理论与新方法。

第二章“大气地表遥感数据验证”利用在轨卫星遥感数据与图像，讨论洪涝、干旱、土壤湿度、植被、积雪、沙尘暴与沙漠化、大气温度湿度廓线、降水、水汽、云水、海洋等中国国土上重要事件的遥感信息研究与应用范例。

第三章“遥感图像处理的人工智能技术”旨在引进人工智能人工生命计算机技术，开展人工智能遥感应用、智能化模式识别与 GIS 专家分析系统的研究。

第四章“多源信息融合”讨论雷达、红外与光、主动与被动等多源数据信息融合的理论与方法，特别是在遥感和目标跟踪信息融合问题中的应用。

第五章“陆面水文过程与遥感信息应用”主要讨论陆地水文环境数字建模与水信息获取，进而开发四维数据同化与遥感信息在水文环境问题中的应用。

第六章“地海环境中目标特性获取”研究地海环境杂波与目标电磁散射信息的复合建模、数值模拟、物理仿真实验与系统。

本项目在立题与研究过程中得到了徐冠华、陈述彭、童庆禧、赵柏林四位中国科学院院士的大力推荐，得到了国家科技部、国家自然科学基金会、上海市科委，以及各课题承担单位的大力支持，我们深表感谢。陈述彭先生在“五一”假日中为我们写了热情洋溢和高屋建瓴的序言，使我们深受鼓舞。我们感到不安的是，我们的工作离开“学术要顶天，应用要立地”的要求还存在不少的距离，大量的问题有待于深入与创新性地突破，任重而道远，需要我们在今后加倍地努力。中国的和平崛起是二十一世纪最伟大的事件，让我们在自己的岗位上为之而奋斗。

金亚秋　2005 年 5 月

（国家 973 项目 2001CB309400 首席科学家）

目录

第一章 遥感机理与遥感信息理论

本章着重当前空间遥感发展前沿课题的基础研究，以地球环境中电磁散射与辐射传输为基础，开展新理论与新方法的研究。同时，针对空间遥感国内外技术进展与数据图像资源，提出定量信息获取与处理的新理论方法和应用范例。

电磁场与波是信息科学技术的物理基础。正是以电磁场与波作为信息传输、信息获取和信息诠释的根本手段，才形成了空对地观测与地球空间遥感、现代通信、广播电视、雷达探测、遥控制导与电子对抗、目标成像与探测识别、全球定位系统 GPS 和地理信息系统 GIS 等信息高技术，也形成了地球观测与环境遥感的信息科学基础理论。

空间遥感是在空间平台上用电磁波与地球大气、地表、海洋环境相互作用的散射和辐射来进行观测。它从可见光摄影开始，经过红外热辐射探测，到 20 世纪 70 年代已发展到微波、毫米波遥感。由于微波的全天候特点，能穿过云层，还可探测地下结构，因此，随着空间分辨率的不断提高，微波遥感已成为空间遥感发展最前沿的技术。通过电磁波（微波、毫米波、红外与光波等）在地球环境中散射、辐射传输与传播，从多源海量数据获取到科学的定量信息转化要有更高层次的研究，包括复杂环境的理论建模、数值模拟与大规模计算、数据传输收集、数据验证、数据挖掘、多维数据同化、多源信息融合、反演算法与结构重构、图像自动智能化处理、数字化信息系统，以及个学科特定的应用问题。从信息定性诠释到信息定量评估，从多源观测融合到形成科学知识和全方位应用，这是现代电磁波信息科学与空间地球系统科学等多学科交叉的前沿科学技术。

本章讨论了三维非均匀散射层矢量辐射传输方程（VRT）的高阶散射与辐射求解。通常的 VRT 建模是平行分层随机介质的一维（1D）VRT、或 2D 或 3D 标量均匀散射介质的 RT。三维非均匀散射介质 VRT 能计算空间非均匀分布随机散射元的高阶散射与辐射。

本章还讨论了非均匀分层密集球粒子（积雪）或非均匀非球形粒子（植被）VRT 矢量辐射传输高阶散射与辐射模拟。也将这一理论方法应用于我国月壤辐射探测的空间遥感有效载荷的研究。

还讨论了 VRT 方程和 RT 方程的逆问题解析理论。与统计方法不同，逆问题的解析理论能揭示和建立问题内在的物理关系。

在全极化散射与 SAR 成像机理方面，提出了非均匀植被的极化脉冲回波 VRT 与时间相关的 Mueller 矩阵解，数值计算了脉冲入射下非均匀植被同极化和交叉极化的双站散射，并用于下垫地表的参数反演，以及非均匀植被下异常散射体的识别。提出了用脉冲波测定树林有效高度的概念性方法。超宽带（UWB）脉冲雷达具有很宽的带宽和相当好的距离分辨率，可获得目标的精细回波响应，增强 RCS 和改进对杂波的抑制，将是今后雷达遥感与目标监测的重要进展。

SAR 全极化散射测量与成像是 20 世纪 90 年代以来形成的最重要的空间遥感技术之一。本章讨论了 SAR 全极化散射的随机介质建模、相干矩阵及其特征值分析，相干矩阵特征值及其信息熵与同极化、交叉极化指数测量值的直接关系等。

讨论了单次飞行全极化 SAR 图像反演地面数字高程（DEM），论证了 ψ 迁移是三个散射 Stokes 参数的函数。提出用倾斜地表水平方位排列产生的图像纹理作形态学细化算法来确定水平方位角，可用一次飞行的 SAR 图像数据得到地形 DEM 的反演。

讨论了多时相 SAR 图像双阈值算法自动识别城市多年发展的变化。

这一领域的研究还可参见我们近来出版的专著，如：

Y. Q. Jin, *Theory and Approach of Information Retrievals from Electromagnetic Scattering and Remote Sensing*, New York: Springer, 2005.

金亚秋，空间微波遥感数据验证的理论与方法，北京：科学出版社，2005。

An Approach of Three-Dimensional Vector Radiative Transfer (3-D-VRT) Equation for Inhomogeneous Scatter Media

Ya-Qiu Jin, *Fellow*, *IEEE*, and Zichang Liang

the Key Laboratory of Wave Scattering and Remote Sensing Information of the Ministry of Education, Fudan University, Shanghai 200433, China

Abstract To solve a three-dimensional vector radiative transfer (3-D-VRT) equation for the model of spatially inhomogeneous scatter media, the finite enclosure of the scatter media is geometrically divided, in both the vertical z and horizontal (x, y) directions, to form very thin multiboxes. The zeroth-order emission, first-order Mueller matrix of each thin box, and an iterative approach of high-order radiative transfer are applied to deriving high-order scattering and emission of whole inhomogeneous scatter media. Numerical results of polarized brightness temperature at microwave frequency from an inhomogeneous scatter model such as vegetation canopy are calculated and discussed.

Index Terms High-order scattering and emission, inhomogeneous media, three-dimensional vector radiative transfer (3-D-VRT).

1. Introduction

TO DESCRIBE multiple scattering, absorption, and emission of radiance intensity, the vector radiative transfer (VRT) equation of the Stokes vector $\bar{I}$ has been studied and applied in broad areas. Conventional VRT is usually for the models of parallel-layered media, i. e., one-dimensional (1-D) VRT equation ($d\bar{I}/dz$)[1],[2]. There have been some studies of two-dimensional or three-dimensional (3-D) scalar RT equations, such as the Monte Carlo method and multimodes approach for radiance of atmospheric discrete clouds[3—6], the discrete-ordinate and finite difference method for the problems of heat transfer[7],[8], and neutron transport, etc. However, in all of these approaches, it has been necessary to assume that the host medium itself is homogeneous, i. e. , extinction, scattering and phase functions are considered to be independent of location within the medium. This fact simplifies the problem somewhat as the inhomogeneity in RT and then requires only a suitable treatment of the lateral sides of the medium and their associated boundary conditions. In advances of polarimetric and radiometric observation in remote sensing and the imaginary technology with an improved high resolution, development of 3-D-VRT ($d\bar{I}/dx$, $d\bar{I}/dy$, $d\bar{I}/dz$) model for spatially inhomogeneous scatter media such as vegetation canopy becomes of great interest[9—11]. However, modeling and numerical solution of 3-D-VRT for inhomogeneous scatter media remain to be studied.

To solve the 3-D-VRT equation for spatially inhomogeneous scatter media and obtain high-order scattering and emission, the finite enclosure of the scatter media is first geometrically divided into many thin boxes, slicing the media in both the vertical z and horizontal (x, y) directions. The zeroth-order emission of each thin box and an iterative approach of high-order radiative transfer via the Mueller matrix solution of VRT in all media boxes are applied to deriving high-order scattering and emission of the whole inhomogeneous scatter media. High-order scattering and brightness

* This article was published in *IEEE Transactions on Geoscience and Remote Sensing*, 2004, 42(2): 355—360.

temperature of the inhomogeneous scatter media in 3-D geometry can be numerically calculated. According to the spatial resolution of the observation to divide the finite enclosure of scatter media, this approach presents a numerical method to obtain high-order scattering and emission of the 3-D models for inhomogeneous scatter media such as vegetation canopy, finite cloud fields, etc.

2. 3-D-VRT equation

A geometric model is shown in Fig. 1, where nonspherical particles are randomly and non-uniformly distributed within random limited space, e. g. , such as random cones (it might be as a model for random tree canopy or others). Suppose that the finite enclosure of the media has the length and width as W_1 and W_2, in the x and y directions respectively, and the height d in the z direction. Note that in this model the top and lateral boundaries of the enclosure are not solid, and the underneath of the bottom surface is a homogeneous half-space (land-) medium. The 3-D-VRT[8],[10],[12] of the random scatter media is written as

$$\begin{aligned}&\left(\cos\theta\frac{\partial}{\partial z}+\sin\theta\cos\varphi\frac{\partial}{\partial x}+\sin\theta\sin\varphi\frac{\partial}{\partial y}\right)\\&\bar{I}(\theta,\varphi,x,y,z)\\&=-\bar{\kappa}_e(\theta,\varphi,x,y,z)\cdot\bar{I}(\theta,\varphi,x,y,z)\\&\quad+\bar{\kappa}_a(\theta,\varphi,x,y,z)\cdot C\bar{T}_1(x,y,z)\\&\quad+\int_0^{2\pi}\mathrm{d}\varphi'\int_0^{\pi}\bar{P}(\theta,\varphi,\theta',\varphi',x,y,z)\\&\quad\cdot\bar{I}(\theta',\varphi',x,y,z)\sin\theta'\,\mathrm{d}\theta'\end{aligned}\tag{1}$$

where $\bar{\kappa}_e$, $\bar{\kappa}_a$ are, respectively, the extinction and absorption matrices, $\bar{P}$ is the phase matrix, and $\bar{T}_1$ is the physical temperature of the scatter media.

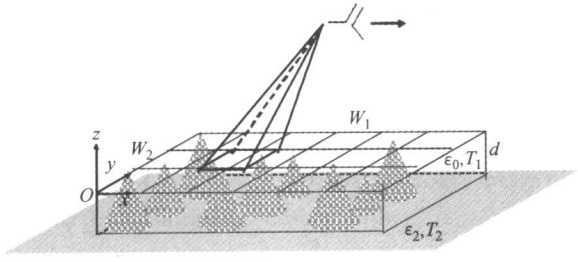

Fig. 1 Geometric model for inhomogeneous scatter media

The boundary conditions at the top ($z=0$) and bottom ($z=-d$) surfaces are written as

$$\bar{I}(\pi-\theta,\varphi,x,y,z=0)=0\tag{2a}$$

$$\begin{aligned}\bar{I}(\theta,\varphi,x,y,z=-d)=&\bar{R}_{12}(\theta)\cdot\bar{I}(\pi-\theta,\varphi,x,y,z=-d)\\&+\bar{T}_{12}(\theta)\cdot C\bar{T}_2\end{aligned}\tag{2b}$$

where $\bar{R}_{12}(\theta)$, $\bar{T}_{12}(\theta)$ are the reflectivity and transmittivity matrices of the bottom surface, respectively. Here, the subscript 12 denotes "between" the random media (1) and underlying medium (2). T_2 is the physical temperature of the bottom medium. Equation (2a) means that there is no downward emission incidence at $(\pi-\theta,\varphi)$ from up-space ($z>0$) to the top surface ($z=0$). Atmospheric radiance is simply not taken into account. Equation (2b) indicates that the upward radiance at the bottom ($z=-d$) is contributed by reflection of downward radiance of the random media and transmitted emission from the underlying medium.

The boundary conditions at the lateral surfaces at $x=0$, $x=W_1$, $y=0$, and $y=W_2$ are respectively written as

$$\begin{cases}\bar{I}(\pi-\theta,\varphi,x=0,y,z)=0\\\bar{I}(\theta,\varphi,x=0,y,z)=\bar{T}_{12}(\theta)\cdot C\bar{T}_2\\\qquad 0^\circ<\varphi<90^\circ,\ 270^\circ<\varphi<360^\circ\end{cases}\tag{2c}$$

$$\begin{cases}\bar{I}(\pi-\theta,\varphi,x=W_1,y,z)=0\\\bar{I}(\theta,\varphi,x=W_1,y,z)=\bar{T}_{12}(\theta)\cdot C\bar{T}_2\\\qquad 90^\circ<\varphi<270^\circ\end{cases}\tag{2d}$$

$$\begin{cases}\bar{I}(\pi-\theta,\varphi,x,y=0,z)=0\\\bar{I}(\theta,\varphi,x,y=0,z)=\bar{T}_{12}(\theta)\cdot C\bar{T}_2\\\qquad 0^\circ<\varphi<180^\circ\end{cases}\tag{2e}$$

$$\begin{cases}\bar{I}(\pi-\theta,\varphi,x,y=W_2,z)=0\\\bar{I}(\theta,\varphi,x,y=W_2,z)=\bar{T}_{12}(\theta)\cdot C\bar{T}_2\\\qquad 180^\circ<\varphi<360^\circ\end{cases}\tag{2f}$$

Equation (2c) indicates that there is no downward incidence from the outside (azimuthally defined by the φ region $0<\varphi<90^\circ$, $270^\circ<\varphi<360^\circ$) to enter the lateral side ($x=0$) of the random media, and the upward radiance from outside comes from the transmitting emission from the underlying half-space medium. Same physical meanings are described by (2d)—(2f) for other lateral sides.

Generally, $\bar{\kappa}_e$ is nondiagonal for nonuniformly (the Euler angles β, γ)[1] oriented scatterers. To find the matrix $\bar{E}$ and its inverse $\bar{E}$, $\bar{\kappa}_e$ can be diagnosed for uniformly γ-oriented ($\gamma\in 0^\circ$, 360°) scatterers as[1],[2],[13]

$$\begin{aligned}\bar{\beta}(\theta,\varphi,x,y,z)=&\bar{E}^{-1}(\theta,\varphi,x,y,z)\cdot\bar{\kappa}_e(\theta,\varphi,x,y,z)\\&\cdot\bar{E}(\theta,\varphi,x,y,z),\end{aligned}\tag{3}$$

where the iith elements of the diagonal $\bar{\beta}$ are denoted

as β_i, $i=1,2,3,4$. It can be known that β_i is the eigenvalues of $\bar{\kappa}_e$, and $\bar{E}$ is composed by the eigenvectors of $\bar{\kappa}_e$. All formulations of $\bar{\kappa}_e$, $\bar{\beta}$ and $\bar{E}$ can be found in [1] and [2].

Left-multiplying $\bar{E}^{-1}$ on both sides of (1) yields

$$\begin{aligned}&\left(\cos\theta\frac{\partial}{\partial z}+\sin\theta\cos\varphi\frac{\partial}{\partial x}+\sin\theta\sin\varphi\frac{\partial}{\partial y}\right)\\&\bar{I}^E(\theta,\varphi,x,y,z)\\&=-\bar{\beta}(\theta,\varphi,x,y,z)\cdot\bar{I}^E(\theta,\varphi,x,y,z)\\&\quad+\bar{\kappa}_a^E(\theta,\varphi,x,y,z)\cdot C\bar{T}_0^E(x,y,z)\\&\quad+\int_0^{2\pi}d\varphi'\int_0^{\pi}\bar{P}^E(\theta,\varphi,\theta',\varphi',x,y,z)\\&\qquad\cdot\bar{I}^E(\theta',\varphi',x,y,z)\sin\theta'\,d\theta'\end{aligned}\tag{4}$$

where

$$\bar{I}^E(\theta,\varphi,x,y,z)=\bar{E}^{-1}(\theta,\varphi,x,y,z)\cdot\bar{I}(\theta,\varphi,x,y,z)\tag{5a}$$

$$\bar{T}_0^E(x,y,z)=\bar{E}^{-1}(\theta,\varphi,x,y,z)\cdot\bar{T}_0^E(x,y,z)\tag{5b}$$

$$\bar{P}^E(\theta,\varphi;\theta',\varphi',x,y,z)=\bar{E}^{-1}(\theta,\varphi,x,y,z)\cdot\bar{P}(\theta,\varphi;\theta',\varphi',x,y,z)\cdot\bar{E}(\theta,\varphi,x,y,z)\tag{5c}$$

$$\bar{\kappa}_a^E(\theta,\varphi,x,y,z)=\bar{E}^{-1}(\theta,\varphi,x,y,z)\cdot\bar{\kappa}_a(\theta,\varphi,x,y,z)\cdot\bar{E}(\theta,\varphi,x,y,z).\tag{5d}$$

For convenience, all notations of E would not be especially indicated in the next derivations.

Let us slice the media enclosure into many thin slabs with the thickness Δd along the z direction, and let us denote the slabs by the subscripts $l=1,2,\cdots,L$ from the top to the bottom. According to the spatial resolution Δh, divide the (x,y) plane of the media enclosure to form many thin rectangular boxes with the length-width Δh and thickness Δd as illustrated in Fig. 2. Because all boxes are very thin, we can assume that the medium within each box is homogeneous. But different boxes can be different, e. g., with different particles, different particle's fractional volumes, or different physical temperatures, etc. It is noted that as the $\bar{\kappa}_e$ and $\bar{P}$ of random particles have been calculated, the approach of VRT of random discrete particles is the same as one of continuous random media no matter what size the particles are comparing with Δd.

As illustrated in Fig. 2, the radiance intensity of the lth slab is defined as

$$\bar{I}_l(\theta,\varphi,x,y)=\begin{cases}\bar{I}(\theta,\varphi,x,y,z=-(l-1)\Delta d) & 0^\circ<\theta<90^\circ\\ \bar{I}(\theta,\varphi,x,y,z=-l\Delta d) & 90^\circ<\theta<180^\circ\end{cases}\tag{6}$$

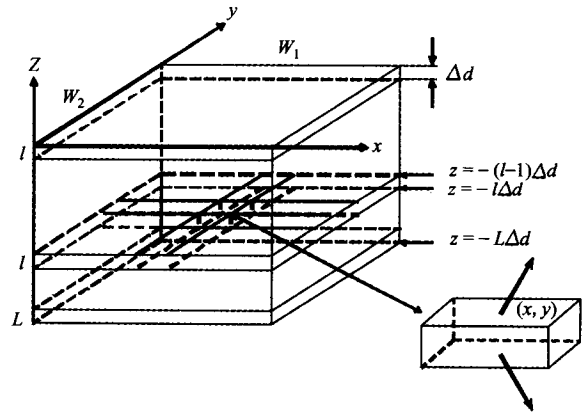

Fig. 2 Dividing the scatter media into multiboxes

where $\bar{I}_l(\theta,\varphi,x,y)$ is the radiance intensity in the direction (θ,φ) from the box of the lth slab whose center is defined at (x,y).

3. Scattering and radiative transfer of 3-D-thin boxes

Because Δd is very small ($\Delta d\ll\Delta h$), change of the radiance intensity through the lateral sides is always much smaller than one through the top and bottom surfaces. Thus, based on VRT [(1)], the changes of up-going ($0^\circ<\theta<90^\circ$) and down-going ($90^\circ<\theta<180^\circ$) radiance intensities through the box of the lth slab whose center is defined at (x,y) are derived as follows:

$$\begin{aligned}&\bar{I}_l^{(n)}(\theta,\varphi,x+\Delta x,y+\Delta y)\\&=\bar{I}_{l+1}^{(n)}(\theta,\varphi,x,y)\\&\quad\cdot\exp[-\bar{\beta}_l(\theta,\varphi,x,y)\Delta d\sec\theta]\\&\quad+\bar{I}_{ls}^{(n)}(\theta,\varphi,x+\Delta x,y+\Delta y)\end{aligned}\tag{7a}$$

$$\begin{aligned}&\bar{I}_l^{(n)}(\theta,\varphi,x+\Delta x,y+\Delta y)\\&=\bar{I}_{l-1}^{(n)}(\theta,\varphi,x,y)\\&\quad\cdot\exp[\bar{\beta}_l(\theta,\varphi,x,y)\Delta d\sec\theta]\\&\quad+\bar{I}_{ls}^{(n)}(\theta,\varphi,x+\Delta x,y+\Delta y)\end{aligned}\tag{7b}$$

where $\bar{I}_{ls}^{(n)}$ is the radiance intensity (self-emission and multiple scattering) happening in the box self, where the superscript n indicates the iteration number [see (9a) and (9b)]. $\bar{\beta}_l=[\beta_{1l},\beta_{2l},\beta_{3l},\beta_{4l}]$ is the vector of diagonal $\bar{\beta}$ of the lth slab.

Radiance transfering from the $(l-1)$th and $(l+1)$th slabs can present the following relations:

$$\Delta x=\tan\theta\cos\varphi\cdot\Delta d$$

$$\Delta y=\tan\theta\sin\varphi\cdot\Delta d.\tag{8}$$

The zeroth-order emission of the box self is

$$\bar{I}_{ls}^{(n=0)}(\theta,\varphi,x,y) = \frac{1-\exp(-\bar{\beta}_l \Delta d|\sec\theta|)}{\bar{\beta}_l} \cdot \bar{\kappa}_{al}(\theta,\varphi,x,y) C\bar{T}_{0l}(x,y). \quad (9a)$$

Multiple scattering from all directions under upgoing and down-going incidences upon the box is

$$\begin{aligned}\bar{I}_{ls}^{(n>0)}(\theta,\varphi,x,y) &= \int_0^{2\pi} d\varphi' \int_{\pi/2}^{\pi} \bar{M}_l(\theta,\varphi,\theta',\varphi',x',y') \cdot \bar{I}_{l-1}^{(n-1)}(\theta',\varphi',x',y')\sin\theta' d\theta' \\ &+ \int_0^{2\pi} d\varphi'' \int_0^{\pi/2} \bar{M}_l(\theta,\varphi,\theta'',\varphi'',x'',y'') \cdot \bar{I}_{l+1}^{(n-1)}(\theta'',\varphi'',x'',y'')\sin\theta'' d\theta'' \end{aligned} \quad (9b)$$

and the relations are also given as

$$x' = x + \frac{\Delta x}{2} + \frac{\Delta d \tan\theta' \cos\varphi'}{2}$$

$$y' = y + \frac{\Delta y}{2} + \frac{\Delta d \tan\theta' \sin\varphi'}{2} \quad (10a)$$

$$x'' = x + \frac{\Delta x}{2} - \frac{\Delta d \tan\theta'' \cos\varphi''}{2}$$

$$y'' = y + \frac{\Delta y}{2} - \frac{\Delta d \tan\theta'' \sin\varphi''}{2}. \quad (10b)$$

The Mueller matrix of the lth slab, $\bar{M}_l$, is approximated by the first-order Mueller matrix, as follows, where the subscripts $i,j=1,2,3,4$.

$$M_{ijl}(\theta,\varphi,\theta',\varphi',x,y) \approx M_{ijl}^{(1)}(\theta,\varphi,\theta',\varphi',x,y) = \frac{P_{ijl}(\theta,\varphi,\pi-\theta',\varphi',x,y)\sec\theta}{\beta_{jl}\sec\theta' + \beta_{il}\sec\theta} \cdot \begin{cases} 1-\exp[-\Delta d(\beta_{jl}\sec\theta' + \beta_{il}\sec\theta)] & 0°<\theta<90°,\ 0°<\theta'<90° \\ \exp(-\beta_{jl}\Delta d\sec\theta') - \exp(\beta_{il}\Delta d\sec\theta) & 90°<\theta<180°,\ 0°<\theta'<90° \\ \exp(\beta_{jl}\Delta d\sec\theta') - \exp(-\beta_{il}\Delta d\sec\theta) & 0°<\theta<90°,\ 90°<\theta'<180° \\ 1-\exp[\Delta d(\beta_{jl}\sec\theta' + \beta_{il}\sec\theta)] & 90°<\theta<180°,\ 90°<\theta'<180° \end{cases} \quad (11)$$

From Fig. 3 and (7a), it can be seen that the radiance $\bar{I}_{l+1}^{(n)}(\theta,\varphi,x,y)$ of the box at the center (x,y) becomes $\bar{I}_l^{(n)}(\theta,\varphi,x+\Delta x,y+\Delta y)$ after propagating and attenuating through this box medium. $\bar{I}_l^{(n)}(\theta,\varphi,x+\Delta x,y+\Delta y)$ will be distributed and enter into the boxes centers of the $(l-1)$th slab based on the ray-projected areas.

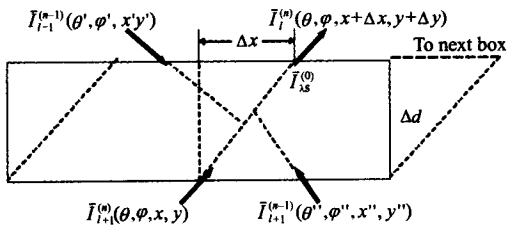

Fig. 3 Illustration of radiative transfer through a box in the zox section

The thin lines with arrows in Fig. 3 indicate the zeroth-order emission $\bar{I}_{ls}^{(0)}$ and multiple scattering from the up and bottom interfaces of the box.

Suppose $\Delta h = 100\text{cm}$, $\Delta d = 1\text{cm}$, the calculation of (8) yields $\Delta x = 16.5\text{cm}$ and $\Delta y = 9.5\text{cm}$ for the direction $\theta = 87°$ and $\varphi = 30°$ (noted that the maximum $\theta_M = \cot^{-1}(2\Delta d/\Delta h) \approx 89°$). The result shows that 0.756 of $\bar{I}_l^{(n)}(\theta,\varphi,x+\Delta x, y+\Delta y)$ remained within the box of the center (x,y), and only 0.079, 0.016, 0.149 of it enter into the neighbor boxes of the centers at $(x,y+\Delta h)$, $(x+\Delta h, y+\Delta h)$, $(x+\Delta h, y)$, respectively. Thus, the radiance intensity through the lateral sides of each box is much smaller than one through the top and bottom interfaces due to very small Δd, and $\bar{I}_{ls}^{(n)}$ of (7) can be calculated by (9a) and (9b).

Now, the steps to calculate brightness temperature emitted from the top interface $\bar{T}_B(\theta,\varphi,x,y,z=0)$ is summarized as follows:

1) By using (9a) and (11), the zeroth-order emission $\bar{I}_{ls}^{(n=0)}(\theta,\varphi,x,y)$ and the Mueller matrix $\bar{M}_l(\theta,\varphi,\theta',\varphi',x,y)$ of each box are calculated.

2) By using the boundary condition (2), calculate the radiative transfer equation (7) from the top surface, the slabs $l=1,2,\cdots,L$ sequentially, and finally to the bottom surface. Adding the emission and reflection of the bottom surface, calculate the radiative transfer equation (7) from the bottom surface, the slabs $l=L,L-1,\cdots,1$ sequentially, and finally to the top surface. Thus, $\bar{I}_{l=1}^{(n=0)}(\theta,\varphi,x,y)$ is obtained.

3) By using (9b), calculate the $(n+1)$th

$(n=0,\cdots)$ order iteration to obtain $\bar{I}_{ls}^{(n+1)}(\theta,\varphi,x,y)$ of each box.

4) Repeating steps 2) and 3) to the Nth iteration, the calculation is finished when $\bar{I}_{l=1}^{(N)}(\theta,\varphi,x,y)$ is small enough.

Let $\bar{I}_{l=1}(\theta,\varphi,x,y)$ is the sum of all iterations $\bar{I}_{l=1}^{(n)}(\theta,\varphi,x,y)(n=0,1,\cdots,N)$, the brightness temperature observed in the up-space is

$$\bar{T}_B(\theta,\varphi,x,y,z=0) = \frac{1}{C}\bar{I}_{l=1}(\theta,\varphi,x,y), \quad 0°<\theta<90°. \qquad (12)$$

4. Numerical results

Suppose that the radiometer's frequency is 3GHz, the scatter particles are prolate spheroids with the semiradii $a=b=0.1$cm and $c=2.5$cm, the dielectric constant of the particle is $\epsilon_s=22+5i$, the fractional volume is 0.0075, and spatial orientation distribution of random particles is uniformly over $\beta\in(30°,60°)$ and $\gamma\in(0°,360°)$. The dielectric constant of the bottom medium is $\epsilon_2=8+1i$. Vertically and horizontally polarized brightness temperatures T_{Bv} and T_{Bh} are calculated.

A. Homogeneous Media

First, compare the results of 3-D-VRT with conventional 1-D-VRT for a homogeneous scatter medium. Suppose that random prolate spheroids uniformly distributed within a rectangular enclosure whose length and width are 15m, and depth $d=1$m. Divide the rectangular enclosure to form thin multiboxes with $\Delta h=1$m, $\Delta d=0.01$m (i.e., 100 thin slabs), and take calculations at discrete angles $\Delta\theta=9°$, $\Delta\varphi=18°$.

From (7) and (9), it can be seen that rigorous calculation is required to store all radiance at different angles (θ,φ) and different centers (x,y) of the boxes. It needs the storage memory about 144MB. When the media enclosure becomes large, the storage memory would be tremendously increased. To reduce such requirement, we propose to use a parabola line to approximately match the radiance of each slab along all direction (θ,φ), and only storage some coefficients of the matching line.

As shown in Figs. 4(a) and (b), three matching points of the parabola line are chosen at $z=0,-d/2,-d$. It only needs to store three coefficients from 100 data, and significantly reduces the storage memory to 4MB. For example, Figs. 4(a) and (b) shows the data of 3-D-VRT from the slabs, respectively, along the line $(\theta=58°,\varphi=9°)$ and $(\pi-\theta=58°,\varphi=9°)$, and good matching by a parabola line.

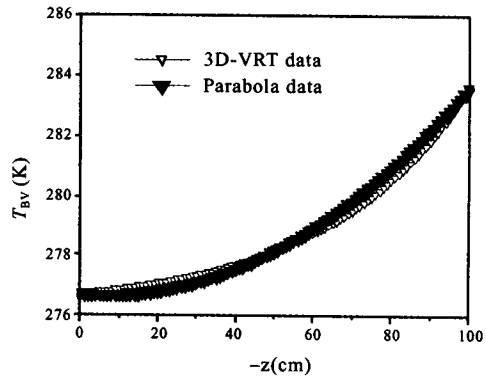

(a)

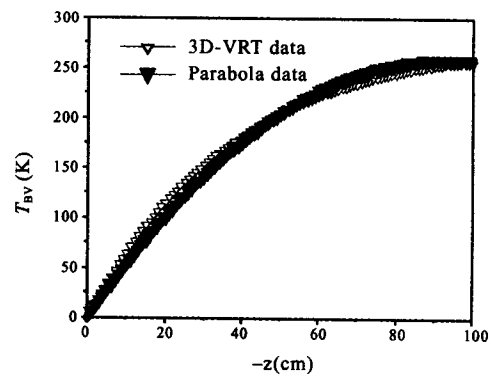

(b)

Fig. 4 Parabola data to match the calculation of 3-D-VRT

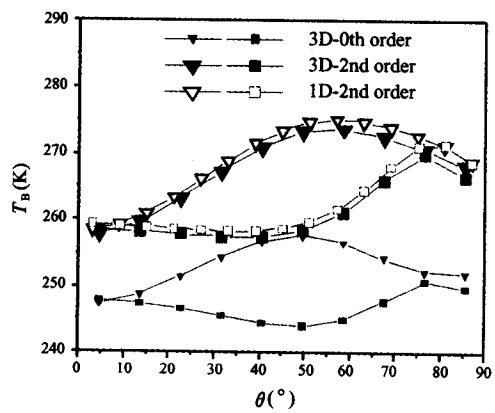

Fig. 5 Brightness temperature from a homogeneous scatter medium

Fig. 5 presents the zeroth-order (small black